Operando multi-edge XAS to unlock the effect of Co in Li- and Mn-rich NMC Li-ion cathodes

Oleg Usoltsev [a], Shehab E. Ali [a,b], Andrea Sorrentino [a], Hyeongseon Choi [d,e], Matthias Kuenzel[d,e], Dominic Bresser [d,e], Stefano Passerini [d,e], Dino Tonti [f], Laura Simonelli [a,*]

[a] *ALBA Synchrotron Light Facility, Carrer de la Llum 2-26, 08290, Cerdanyola del Vallès, Spain*

[b] *Physics Department, Faculty of Science, Suez Canal University, Ismailia, Egypt*

[d] *Helmholtz Institute Ulm (HIU), Helmholtzstrasse 11, 89081, Ulm, Germany*

[e] *Karlsruhe Institute of Technology (KIT), PO Box 3640, 76021, Karlsruhe, Germany*

[f] *Institut de Ciència de Materials de Barcelona (ICMAB), CSIC, Carrer dels Til·lers sn, 08193 Bellaterra, Spain*

*Corresponding author: lsimonelli@cells.es

ABSTRACT

Thanks to their high voltage and delivered capacity, Li-rich transition metal (TM) oxide positive electrode (cathode) materials are among the most promising for next-generation lithium-ion-batteries, where Co-free Li-rich cathodes join reduced costs with competitive performance. However, their cycle-life remains limited, and the individual role of TMs is still not fully understood. The investigation of the TM chemical species' evolution along the first charge for $Li_{1.2}Mn_{0.56}Ni_{0.16}Co_{0.08}O_2$ and $Li_{1.2}Mn_{0.6}Ni_{0.2}O_2$ has been accessed by means of *operando* multi-edge XAS. The charge compensation mechanism has been studied and the effect induced by removing Co has been revealed. The absence of Co results in an accelerated and completed Ni oxidation along the first stage of charge and an inhibited formation of the undesired spinel phase and oxygen release at the end of the high voltage plateau. Interestingly, the oxygen release in the Co-containing material involves mainly the oxygen close to the Mn site and occurs while local structural interlayer re-arrangements are taking place.

INTRODUCTION

The development of effective and sustainable energy storage is nowadays a societal challenge to mitigate the CO_2 concentration increase in the Earth's atmosphere and possibly to allow its reduction in the next decades[1]. Despite the relative scarcity of lithium and other raw materials, Li-ion batteries (LIBs) are the most remarkable success case in the energy storage technology landscape of (at least) the last fifty years. Lithiated layered transition metal (TM) oxides are widely used as positive electrode (cathode) materials in LIBs, because they offer high energy density and reversibility, while being relatively safe[2, 3, 4], and their flexible composition allows for a fine tuning of performance and properties[5]. Since their appearance in the market, the most limiting performance factors for LIBs are cost and gravimetric & volumetric capacity limits.

For this class of materials, $LiCoO_2$ is considered the basis layered compound, for which the delithiation process in a $LiCoO_2$/C Li-ion cell is limited to around 140-160 mAh g^{-1} [6], while relatively high costs are related to the critical cobalt[7, 8]. To go beyond this limit, chemical substitutions at the Co sites have been explored, enhancing the maximum energy density and decreasing at the same time the production costs and safety hazards. In particular, the Co^{3+} partial substitution by Mn^{4+}, Ni^{2+}, and Li^{+} ions, enhances the electrochemical properties, resulting in a new layered cathode material called "Li-rich NMC". This approach combines the different properties and effects of Ni, Co and Mn with the possibility of storing additional Li in the TM layers, showing capacities exceeding 280 mAh g^{-1} [9], i.e., much higher than that of conventional $LiCoO_2$. Despite the great potential, Li-rich NMCs suffer poor kinetics and voltage decay upon cycling. To reduce these problems, many efforts have been made. In particular, changes in the combinations of different cation ratios[10, 11, 12], charge[13, 14], temperature and cooling processes[15, 16, 17], different reagents and coatings[18, 19, 20, 21, 22, 23] have been studied. Despite this, the full understanding from the structural/chemical point of view is still not complete for a rational design of new materials. The occurrence of an initial activation process during the first delithiation step is always accompanied by a large irreversibility in terms of capacity, while the exceeding oxidation of nickel and cobalt and reversible and irreversible oxygen electrochemistry occurs[24, 25, 26, 27]. Moreover, Mn is redox-active and shows a partial reduction from Mn^{4+} to Mn^{3+} in both high and low spin configurations along the first charge, where the former corresponds to a partial irreversible spinel formation and the latter is expected to favor reversible cycling[28, 29]. This requires oxygen oxidation to an even higher extent, making the charge compensation mechanism in these

materials particularly complex, involving both the cationic and anionic contributions with overlapping reversible and irreversible processes. Indeed, the detected O_2 release at the end of the first charge, or the eventual generation of partly reduced oxygen species (such as O^-, O_2^{n-} (n<4), and other radicals) leads to dramatic structural and/or electronic changes in the material, making complex the attribution of the redox processes involved. In this scenario *operando* studies become a key. Indeed, *operando* techniques allow the correct correlation of the observed evolution with the electrochemistry, enabling the detection of metastable intermediates and ensuring the characterization under real conditions (non-equilibrium) avoiding the risk of *ex-situ* sample evolution during manipulation. *Operando* experiments are thus needed for both the elucidation of redox mechanisms and also the understanding of failure processes. Synchrotron radiation-based techniques are powerful tools for battery research and allow for probing a wide range of length scales[30, 31].

Recently, the specific role of the different cations in the behavior of Li-rich NMC has been increasingly of interest[32]. Indeed, it is especially relevant in the efforts to reduce the reliance on critical cobalt in lithium batteries. The concept of Li- and Ni-rich[33, 34] and Co-poor or Co-free[35] cathodes have evolved as the most promising ones. The mechanisms involved in the absence or the presence of a minor amount of Co is here addressed, by comparing $Li_{1.2}Mn_{0.56}Ni_{0.16}Co_{0.08}O_2$ with $Li_{1.2}Mn_{0.60}Ni_{0.20}O_2$ via *operando* X-ray absorption spectroscopy (XAS) at the Mn, Ni and Co *K*-edges, complemented by *ex-situ* full field transmission X-ray microscopy (TXM) at the O *K*-edge and Mn L_3-edge. The results obtained allow for following the electrochemically driven evolution of the electronic and local structure around the different cations, addressing the different phases evolution thanks to advanced statistical data treatments.

EXPERIMENTAL METHODS

Material synthesis and coin cell preparation. $Li_{1.2}Mn_{0.56}Ni_{0.16}Co_{0.08}O_2$ and $Li_{1.2}Mn_{0.60}Ni_{0.20}O_2$, later addressed as Co08 and Co00, were synthetized by co-precipitation followed by a solid-state reaction, using the transition metal acetates and $LiOH{\cdot}H_2O$ as precursors[36]. The electrode composition was 85 wt% LR-NMC, 10 wt% conductive carbon (Super C65, IMERYS) and 5 wt% binder (polyvinylidene difluoride, PVdF, Solef 6020, Solvay). To prepare the electrodes, PVdF was first dissolved in *N*-methyl-2 pyrrolidone (NMP). Then, the active material (Co00 or Co08) and the conductive carbon were introduced in the PVdF solution. The resulting slurry was cast on

Al foil, which was dried at 80 °C in oven for 3 h and then kept at room temperature in a dry room (dew point < -70 °C) overnight. Disk-shaped electrodes with a diameter of 12 mm were punched out of the electrode sheets, pressed at 10 t for 10 s, and dried at 120 °C and pressure of 10^{-3} mbar for 14 h. The active material mass loading was around 3.0-3.5 mg cm^{-2} [37].

For the *ex-situ* TXM measurements, Co00 or Co08 electrodes were cycled in two-electrode pouch-type cells assembled in the dry room (dew point < 70 °C). The cells employed lithium metal foil (Honjo, battery grade) as the negative electrode. Whatman glass fiber sheets (GF/A) served as the separator and were drenched with 100 µL of the electrolyte (1 M $LiPF_6$ in a 1:1 weight mixture of ethylene carbonate and dimethyl carbonate, UBE). The galvanostatic cycling was conducted using a battery tester (Maccor 4300), setting the anodic and cathodic cut-off potentials to 4.8 and 2.5 V, respectively. A dis-/charge rate of 1C corresponds to a specific current of 200 mA g^{-1}. The cells were fully charged and then disassembled in an argon-filled glove box. In order to minimize the contribution of the conducting salt or other possible soluble species from the electrolyte, the samples were rinsed with dimethyl carbonate (UBE) and the active material was recovered from the electrodes.

For the *operando* hard X-ray absorption spectroscopy (XAS), the electrodes were loaded into coin cells modified with 75-µm-thick Kapton windows to allow for photon transmission. A Li foil was used as negative electrode and standard $LiPF_6$ in the 1:1 (w:w) mixture of ethylene carbonate and dimethyl carbonate as electrolyte soaking a glass fiber filter used as separator.

Hard X-ray absorption measurements. *Operando* Mn, Co, and Ni *K*-edge XAS spectra were acquired at the CLÆSS beamline of the ALBA synchrotron (Spain)[38]. The synchrotron radiation emitted by a wiggler source was monochromatized using a double crystal Si(111) monochromator. The higher harmonics' have been rejected by choosing proper angles and coatings of the collimating and focusing mirrors. The spectra were recorded in transmission mode by means of two ionization chambers while cycling two cells in parallel. A beam-size of 0.4 x 0.7 mm^2 was exploited and the multi-edge measurements on two coin cells where alternated along the cycling. The pristine state, the beginning (charge to 100 mAh g^{-1}) and the end (charge to 200 mAh g^{-1}) of the high-voltage plateau, and the fully charged state as well as the subsequently discharged state were also measured *ex-situ* for a direct comparison with the *operando* measurements. In this case, several spectra were measured to ensure their reproducibility and to obtain a high signal-to-noise-ratio.

The XAS spectra were treated involving a standard procedure based on the cubic spline fit to the pre-edge subtracted absorption spectra to extract the extended X-ray absorption fine structure (EXAFS) signal[39]. Prior to this, the data were calibrated, normalized and deglitched using the in-house developed software named FDA. The Mn, Ni, and Co phases evolution have been monitored on the XANES spectra applying multivariate curve resolution-alternating least squares (MCR-ALS) unmixing, using the MCR toolbox[40, 41]. The EXAFS signals were fitted using original code exploiting the xraylarch python library[42]. The coordination number, Debye-Waller parameter and interatomic distances were obtained for fitting with MnO_2, NiO and CoO_2 theoretical models. The "Hanning" window was applied to the $\chi(k)$ functions with k-ranges of [3-11] $Å^{-1}$ for Mn *K*-edge, [3-8] $Å^{-1}$ for Ni *K*-edge and of [3-8] $Å^{-1}$ for Co *K*-edge were selected. In all cases the fitted R-range was set to [1-2] Å. The EXAFS oscillations have been modeled considering only the first shell contribution, with the number of free fitting parameters remains always below the intrinsic limit defined by the Nyquist theorem[39]. The averaged interatomic distances (R_{Mn-O} or R_{Ni-O}), their corresponding mean square relative displacements (σ^2) representing the local structural disorder, and the coordination number (N) have been considered as variables in the Mn *K*-edge fits, while N have been found always close to 6 for the Ni *K*-edge modelling and have been fixed to such value for the reported results.

Energy-resolved soft X-ray transmission microscopy. Ex-situ spectromicroscopy was performed at the MISTRAL beamline of the ALBA Synchrotron[43] at the O *K*- and Mn L_3-edges. The cathode materials were scraped from electrodes, suspended in dimethyl carbonate (Sigma-Aldrich) and drop-casted on carbon-coated Au TEM grids inside an Ar-filled glovebox. The grids were then mounted on the sample holders and transferred in the MISTRAL microscope in Ar atmosphere to avoid any air contamination. Inside the microscope samples were kept at cryogenic temperature ($T < 110$ K) and under high vacuum conditions during all the measurements. The inorganic particles appeared well distributed on the carbon surface and their size was well above the instrument lateral resolution of about 30 nm half pitch. Representative regions of the samples were selected from 100 μm × 100 μm "mosaic" images recorded on different zones of the grids as composition of many 12 μm × 12 μm fields of view (FOVs) just at two energies, above and below the Mn L_3-edge for a first localization of manganese compounds. FOVs with good particle dispersion were selected for the acquisition of the energy stack. Transmission FOV images (2 s exposure time, effective pixel size 12 nm) were collected, varying the energy across the O *K*- and

Mn L_3-edge with a variable spectral sampling (0.5−0.1 eV). The energy resolution was determined at the nitrogen *K*-edge measuring the visibility of nitrogen gas peaks at the exit slit of the monochromator following the strategy proposed in ref.[44]. The energy resolution at the Mn L_3-edge was extrapolated to be around 0.5 eV (full width at half maximum). A preliminary calibration of the absolute value of the energy was carefully performed before the experiment using standard references samples at different energies along the available energy range of the beamline ($CaCO_3$, N_2, TiO_2, Mn_2O_3, and Fe_2O_3). The necessary total acquisition time for a single energy stack of transmission images was about 1 h.

RESULTS AND DISCUSSION

The quasi-simultaneous XANES *operando* spectra collected at the Mn and Ni *K*-edge of $Li_{1.2}Mn_{0.56}Ni_{0.16}Co_{0.08}O_2$ (Co08) and $Li_{1.2}Mn_{0.60}Ni_{0.20}O_2$ (Co00) are reported in Fig. 1, while the Co *K*-edge spectra obtained for Co08 and their analysis are depicted in Fig. S2, S3, and S4 of the supporting information. The corresponding electrochemical curves over the first cycles, showing the superior capacity retention of Co00 compared to Co08, are reported in Fig. S1. Comparing the two systems, despite the similarity of the two pristine states to $LiNi_{1/3}Mn_{1/3}Co_{1/3}O_2$ (Fig. S5), larger spectral evolutions as a function of the first charge are evidenced at the Mn *K*-edge of Co08, while stronger spectral evolutions are visible at the Ni *K*-edge of Co00.

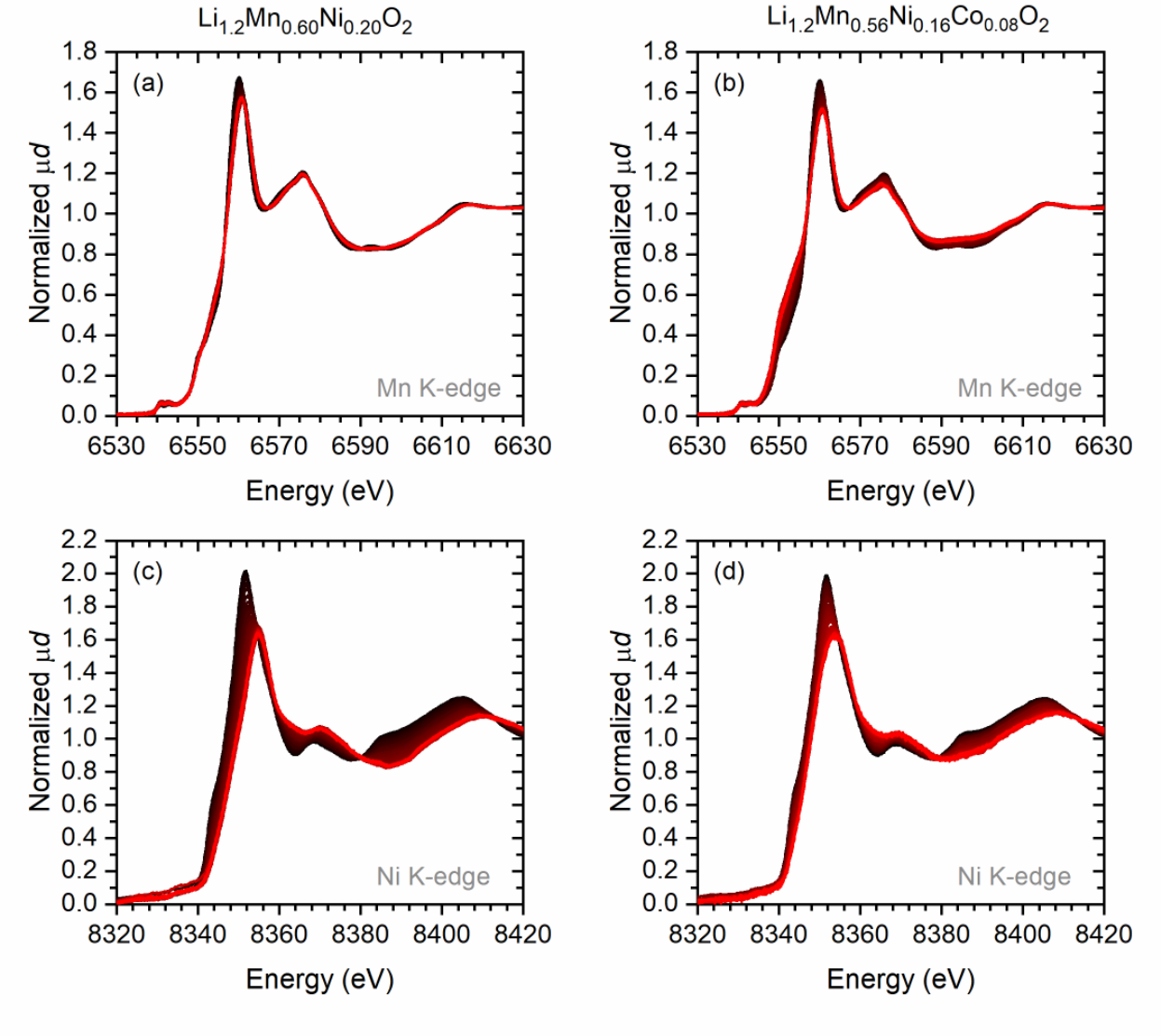

Figure 1: Evolution of the Mn (top) and Ni (bottom) *K*-edge XANES spectra collected over $Li_{1.2}Mn_{0.60}Ni_{0.20}O_2$ (left) and $Li_{1.2}Mn_{0.56}Ni_{0.16}Co_{0.08}O_2$ (right) cathodes along the first charge, where the black (red) color corresponds to the pristine (charged) state.

While the pristine and charged states overlap with the corresponding *ex-situ* spectra (Fig. S6) and agree with the literature[13, 28], this is not the case for the first discharged state. Indeed, along the measurements, the electrolyte close to the irradiated part of the cathodes progressively dried out, limiting the investigation to the first charge, as shown by the evolution of the absorption jump in Fig. S7. Nonetheless, the continuous decrease of the absorption jumps and the comparison with the *ex-situ* data along the first charge (Fig. S6) support the significance of *operando* data in characterizing the electrochemical behavior.

To deconvolute each *operando* spectra data set in its major components, the multivariate curve resolution (MCR) approach was applied. The spectra of the chemical components resolved by MCR are displayed in Fig. 2a and d for the Mn and Ni *K*-edge XANES spectra, respectively, and are compared with the $LiNi_{1/3}Mn_{1/3}Co_{1/3}O_2$ and $LiMn_2O_4$ references in Fig. S8. At the Mn *K*-edge, the first identified component, the gray curve, corresponds to the pristine state, while the other two components are needed to describe the spectral evolution as a function of delithiation in both Co00 and Co08 electrodes. The second component (red curve) could resemble the Mn spinel phase, which is known to form in Co08 along the first charge[28], but its spectral shape shows significant differences with respect to the $LiMn_2O_4$ reference, making this assignment not straightforward. Moreover, by looking to the evolution of the MCR components weight as a function of the Li content (Fig. 2b,c) it seems that Co08 contains a significant amount (20%) of the second component already at the pristine state, which becomes the major one (70%) in the charged state. Previous studies based on EXAFS fits on the same material quantified the formation of the spinel phase up to only 10% during the first charge[28]. It is possible that this second component corresponds to the overlapping contribution of the spinel formation and some structural stack changes. Indeed, similarly to the $LiCoO_2$ case, the detected spectral variation around 6553 eV could correspond to a different level of random stacking sequence of the layered structure and those of Li/Mn arrangement in ordered rocksalt polymorphs[45, 46]. Finally, the third MCR component corresponds to the delithiated state in Co00, where the local lattice compression due to the Li removal could correspond to the detected shift toward higher energies of the main absorption feature[24, 32]. At a charge capacity of around 140 mAh g^{-1}, the Mn *K*-edge spectral component corresponding to the pristine state is still the major one in Co08 while it is already the minor one in Co00, suggesting an accelerated response to the delithiation in the latter material (Fig. 2b,c). At the same time, the Mn *K*-edge spectra collected on Co00 as a function of the first charge could be represented with only two main components, the pristine state component almost fully transforming in the third component representing the charged state, where the additional one (second component, red curve in Figure 2a) most likely accounts for less than 10% of spinel formation above 200 mAh g^{-1}. Instead, the spectral evolution in Co08 seems more complex. Indeed, the initial state only partially transforms into the charged contracted state. The second component evolution accounts for the expected 10% of spinel formation[24], to which most likely the step like behavior around 130 mAh g^{-1} corresponds, and probable stacking re-arrangements[32].

The second component, differently from the Co00 case, strongly increases above 250 mAh g^{-1} at the expense of the delithiated state, most likely because of structural rearrangements.

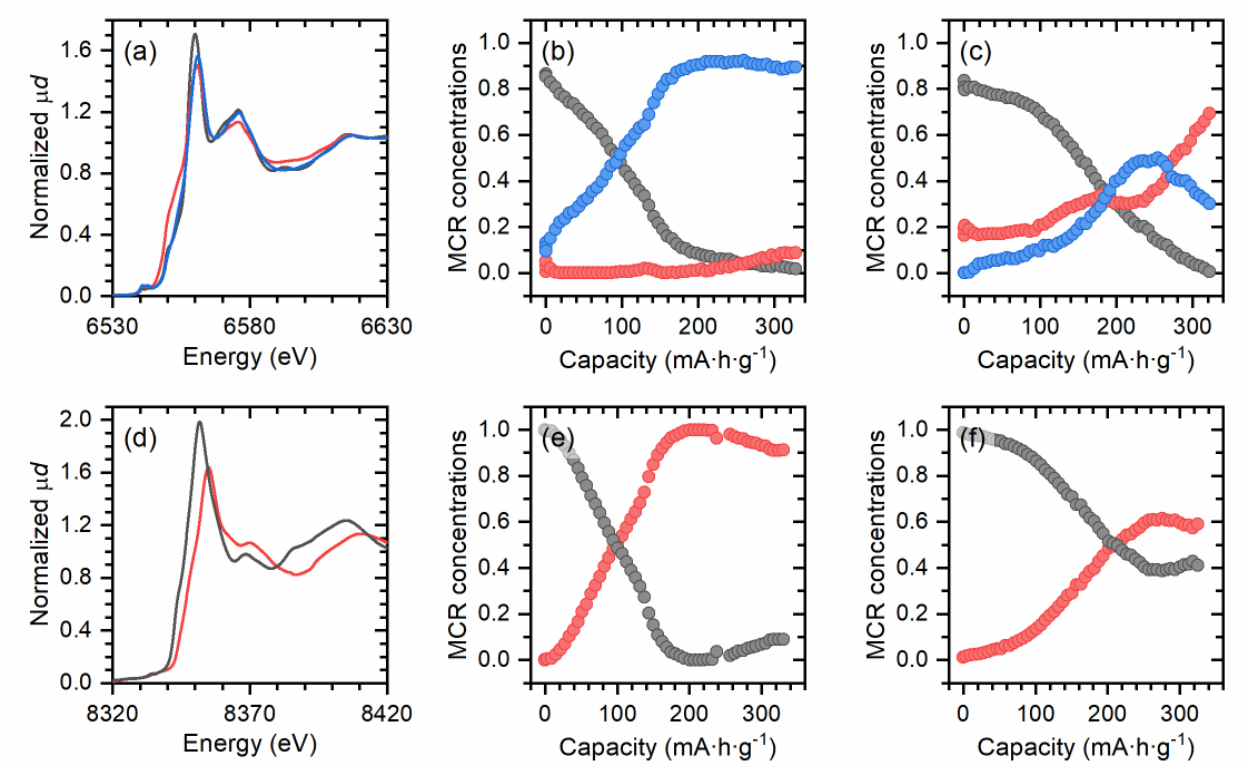

Figure 2: (a) MCR components of the *operando* Mn (a) and Ni *K*-edge (d) absorption spectra and their evolution for the Co00 (b,e) and Co08 (c,f) cathodes. Respective scree plots are presented in Fig. S9.

The spinel formation has been confirmed by *ex-situ* accessing the Mn L_3-edge, where a shift of the first absorption feature toward lower energy is visible already with a minor spinel formation[28]. The Mn L_3-edge spectra, collected on the pristine and charged states by means of transmission X-ray microscopy (TXM), are reported in Fig. 3, left and middle panels. Both spectra corresponding to the pristine state mainly indicate for a Mn^{4+} phase, while both spectra collected in the charged state present a tiny shift of the first absorption feature toward lower energy in agreement with a partial Mn reduction, which can be associated to the minor spinel formation. The direct comparison of the charged state of Co00 and Co08 indicates a slightly larger spinel formation in the latter material, as shown in Fig. 3 middle panel. The TXM image reported in Fig. 3 right panel corresponds to Co00 in the charged state and has been obtained through the formula: $(y - y_{pre})/(y_{post} - y_{pre})$, where y is the TXM image collected at 642 eV and y_{pre} and y_{post} represent the images

collected before and after the edge at 638.8 and 642.6 eV, respectively. Pixels not containing Mn or with a too high absorption (peak at 642 eV < 2) have been dark-shadowed. The regions corresponding to a shifted first absorption feature toward lower energy, i.e., corresponding to the spinel formation, appear brighter in this image. Despite the limited number of isolated particles, it seems that the spinel formation is happening at the particle surface in the Co-free material, an effect that we were not able to observe for Co08, where the spinel rather seems to form in the bulk of the particles[28-29]. This, together with a detected global reduced spinel formation in Co00 when compared with Co08, is in agreement with the proposition that Co favors fast kinetics of TM migration along the charge process[32]. In particular, the TXM data suggest a possibly reduced Mn migration in the Co-free material. Comparing the herein reported results for $Li_{1.2}Mn_{0.56}Ni_{0.16}Co00_{.08}O_2$ with those obtained for $Li_{1.2}Mn_{0.4}Co00_{.4}O_2$[32], where the latter was containing around 4 times more Co, it seems possible to generalize the above reported Co effects in Li-rich NMC cathodes, despite the typical high variability of the performance of this class of cathodes as a function of different TM compositions.

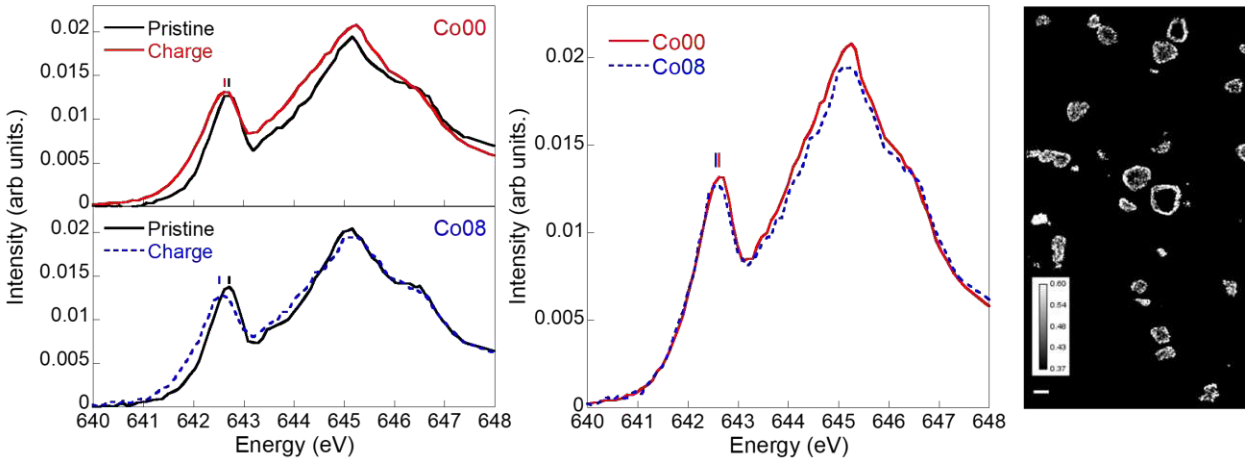

Figure 3: (left) Mn L_3-edge spectra collected on the pristine and charge state of the Co00 and Co08 electrodes. (middle) Comparison in between the spectra collected on the two charge states. (right) Normalized TXM image collected at 642eV, considering as pre- and post-edge energies 638.8 and 642.6 eV, respectively. The scale bar in the bottom left corresponds to 120 nm. Brighter regions correspond to the zones where a partial Mn reduction occurred.

Also, the Co *K*-edge XANES data collected on Co08 can be represented by 3 components (Fig. S3): a first one (grey line) corresponding to the pristine state (Co^{3+}), a second one (red line) to variations in the stacking arrangements[45], and a third one (blue line) to the charged state (Co^{4+}). The pristine component is almost fully converted on the ones representing the charged state with a behavior correlating with the Mn *K*-edge components detected on the same cathode. Interestingly, at the end of the charge process, the oxidized component is decreasing in favor of the second one, suggesting, as at the Mn *K*-edge, local interlayer structural rearrangements occurring in Co08 above 240 mAh g^{-1}, most likely corresponding to the O_2 release that occurs at the end of the voltage plateau.

Instead, the Ni *K*-edge data set can be represented with only two components for both Co00 and Co08. Such two components correspond to Ni^{2+} and Ni^{4+} species, with the former being present in the pristine state, while the latter exists in the charged state. Interestingly, the Ni oxidation seems almost complete at 140 mAh g^{-1} in Co00, while it just started in Co08 (Fig. 2, panel e and f), and it correlates to the first-to-third component transformation shown at the Mn *K*-edge. Indeed, Ni^{2+} almost fully oxidizes to Ni^{4+} along charge in Co00, while it seems to not entirely oxidize in Co08. This is supported by the O *K*-edge pre-peak presented in Fig. S10, where a tiny shifts toward higher energy of the feature around 533 eV is a signature of remnant Ni^{2+} in Co08. The Ni oxidation induces a strong local contraction of the Ni-O shell, which is expected to induce strains on the Mn network[24], probably at the origin of the reported correlation in between the spectral components evolution reported for the two absorption edges.

Consistently with the previously reported results, the detected TM oxidation does not fully justify the experimentally measured capacity, but O oxidation is taking place along the charge[24]. Interestingly, in the absence of Co, the early occurring Ni oxidation limits the oxygen redox to the voltage plateau, while in Co08 both the cation and anion oxidation contribution are present and comparable at the beginning of the charge plateau (starting around 120 mAh g^{-1}), which is in good agreement with previous results[24]. This could be related to the local different stacking arrangements in the two pristine materials and how they evolve upon charge, where low-defect samples are expected to convert faster to the spinel phase, seriously affecting cycling stability, while higher capacities are achieved with highly defective samples[46]. Within this consideration, it is tempting to deduce that Co00 presents higher defects, i.e., a higher amount of random stacking sequences of the layered structure compared to Co08.

The quasi-simultaneous, *operando* EXAFS spectra collected at the TM *K*-edge on Co08 and Co00 allow for accessing quantitative details of the local structural evolution around the absorbers and as a function of the first charge. In Fig. 4, the Fourier transforms of the k^2 weighted EXAFS oscillations collected at the Mn and Ni *K*-edges and on both systems are displayed, and the Fourier transforms of the k^2 weighted EXAFS oscillations collected at the Co *K*-edge on the Co08 cathode are presented in Fig. S2b.

The first peak around 1.4 Å corresponds to the TM-O shell, while the contribution around 2.5 Å corresponds to the TM-TM bond. At the Mn *K*-edge, the charge induces a damping of both the first and second shell contribution in both materials, with a stronger spectral variability for the Co08 system. The minor intensity decrease of the Mn–TM contribution in the Co-free sample could correspond to an improved structural stability and slower oxygen release[47]. At the Co *K*-edge, the charge induces a damping of both the first and second shell contribution similarly to the Mn *K*-edge collected on the same Co08 cathode. At the Ni *K*-edge, the Fourier transform evolution as a function of charge shows clear differences for the two systems, where a strong structural disorder increase characterizes the Co08 spectral evolution toward a contracted charge state. Instead, the Ni-TM contribution intensity for Co00 seems to be not affected by the charge, while the Ni-O shell contracts.

The EXAFS fitting results are presented in Figs. 5, 6, and S4 for the Mn, Ni, and Co *K*-edge results, respectively.

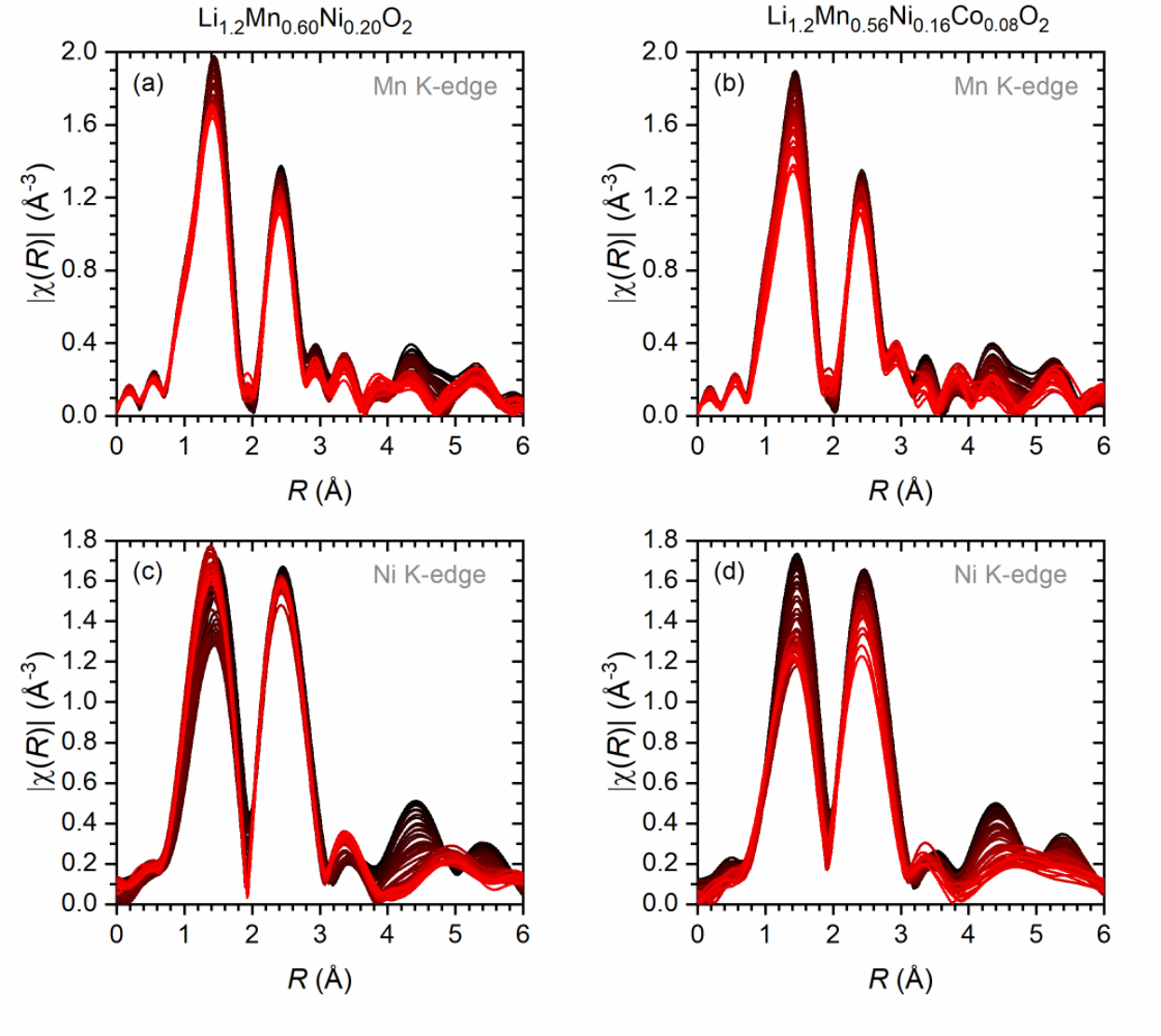

Figure 4: Evolution of the Mn (top) and Ni (bottom) Fourier transform of the k^2 weighted EXAFS oscillations collected from $Li_{1.2}Mn_{0.60}Ni_{0.20}O_2$ (left) and $Li_{1.2}Mn_{0.56}Ni_{0.16}Co_{0.08}O_2$ (right) cathodes along the first charge, where the black (red) color corresponds to the pristine (charged) state.

The Mn-O shell contracts in both materials upon charge (Fig. 5a,d), consistently with the shift toward higher energies of the main XANES feature. Generally, a shorter Mn–O bond implies a higher Mn–O covalence, which in fact results from a greater charge transfer from oxygen in Li-rich NMC materials[24]. This can activate the oxygen redox, potentially generating highly unstable oxygen species, so as to contribute to the oxygen release and poor thermal stability[47]. Interestingly, while the Mn coordination number N is constant for Co00, it decreases for Co08 above 240 mAh

g^{-1} (Fig. 5 b and e), which is consistent with the O_2 release that was evidenced at the end of the voltage plateau for this system[27, 48]. This suggests the suppression of the oxygen release for the Co-free material, in agreement with the detected reduced Mn migration along the charge. Finally, the parameter defining the local disorder (σ^2) increase upon charge correlates with the Mn *K*-edge XANES first and third component exchange behavior (Fig. 2b,c), indicating higher local structural disorder in the charged state.

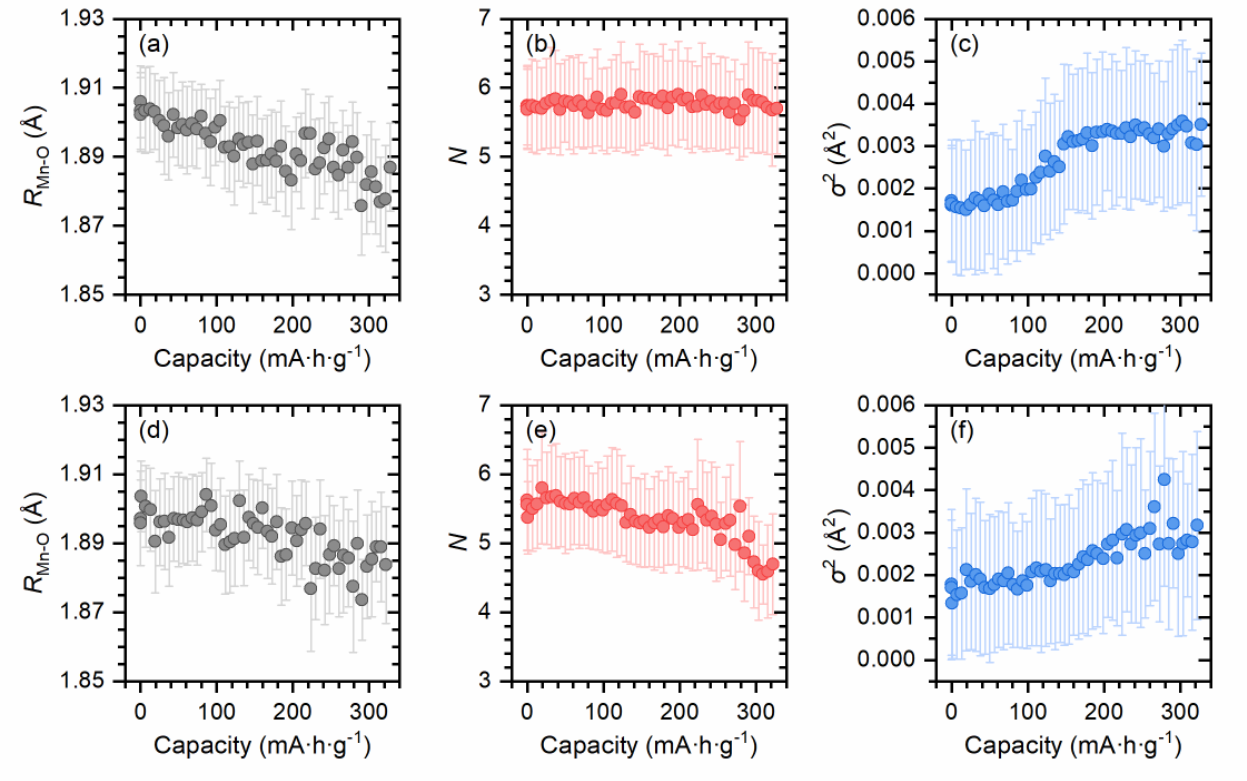

Figure 5: Evolution along the first charge of the Mn-O interatomic distance (R_{Mn-O}), corresponding coordination number (N), and mean square relative displacement (σ^2) for Co00 (top) and Co08 (bottom).

The Co-O shell slightly contracts while, interestingly, its local structural disorder increases above 240 mAh g^{-1} (Fig. S4), correlating with the O_2 release and the local interlayer structural rearrangements occurring close to both the Mn and Co sites, suggesting their proximity and relative influence.

The Ni-O shell strongly contracts as a function of charge, at lower capacity and in higher amount for Co00, in agreement with the full change in the Ni oxidation state from 2+ to 4+. The evolution as a function of specific capacity of R_{Ni-O} for both systems directly correlates with the Ni *K*-edge

XANES components evolution along charge (Fig. 2 e, f) and the Mn-O local structural disorder (Fig 5c, f). The Ni-O shell σ^2 parameter increases in both systems, but to a lower extent for Co00, while a peak is evidenced where both Ni^{2+} and Ni^{4+} oxidation states coexist, which is in agreement with the existence of two different Ni-O shells corresponding to the two Ni oxidation states. Instead, the σ^2 parameter increases with a step-like behavior for Co08, suggesting the coexistence of the two oxidation states at the end of the charge process, in agreement with the XANES results (Fig. 2f). In the error bar, no local interlayer structural rearrangements can be hypothesized close to the Ni sites, suggesting its minor role in the undesired oxygen release.

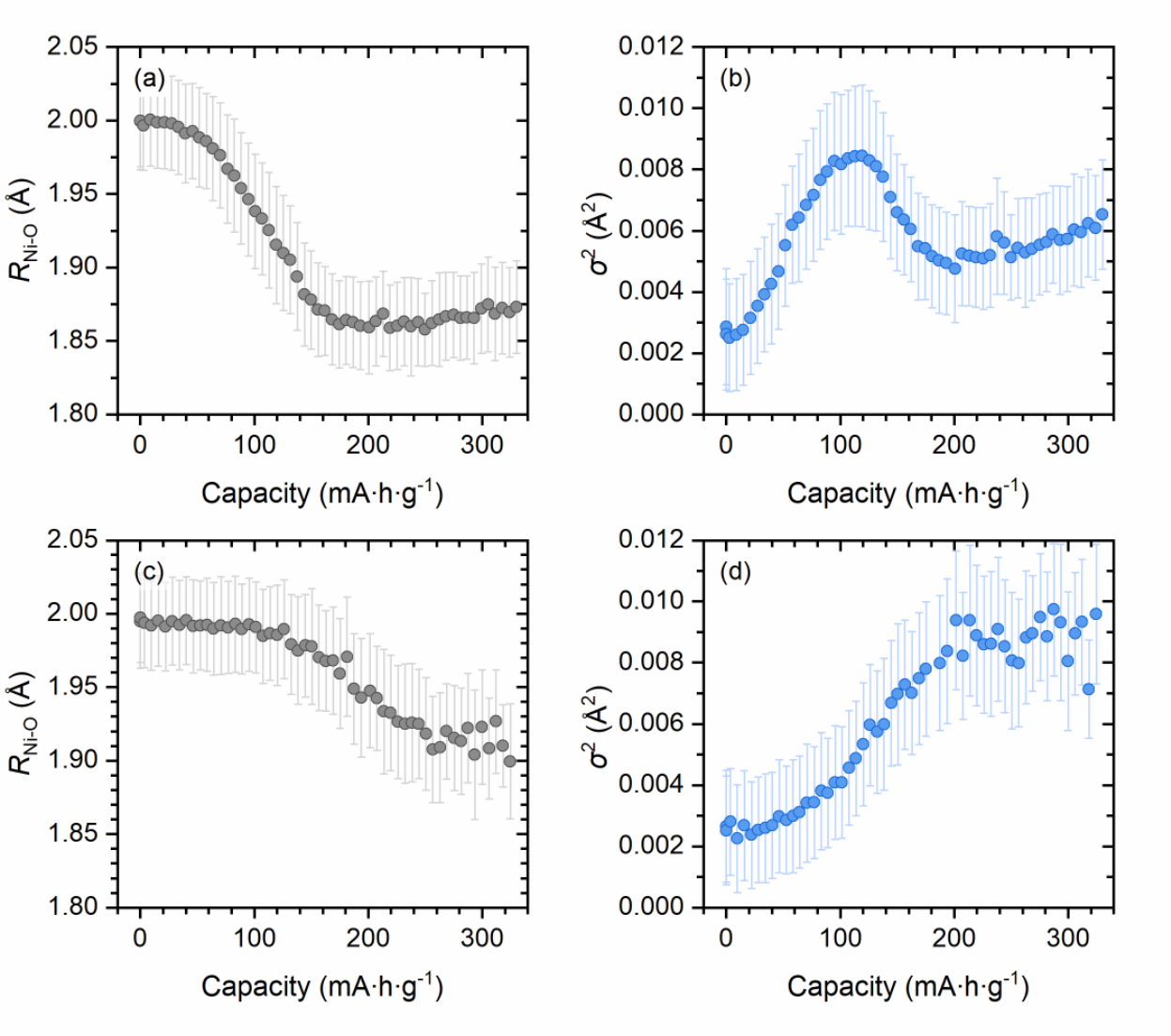

Figure 6: Evolution along the first charge of the Ni-O interatomic distance (R_{Ni-O}), corresponding coordination number (N), and mean square relative displacement (σ^2) for Co00 (top) Co08 (bottom).

CONCLUSIONS

The *operando* evolution of the Mn, Co and Ni *K*-edge absorption spectra have been investigated on Li- and Mn-rich cathodes, focusing on the effect of Co in the transition metal layer. Clear correlations have been identified from the TM response to the first charge, where the absence of Co is anticipating and completing the TM reactions in accordance to the better performance. While Ni is oxidized from 2+ to 4+ along the first charge, Mn is mainly maintaining its 4+ oxidation state, and, in Co08, Co is oxidized from 3+ to 4+. The early Ni oxidation in Co00 limits the oxygen redox to the voltage plateau, while only in Co08 both the cationic and anionic contributions are present and comparable at the beginning of the charge. Only around 10% of Mn spinel phase has been detected to form along the first charge and it seems reduced by the absence of Co in the inner part of the cathode material particles, confining its formation to the particle surface. Interestingly, the absence of Co affects the local interlayer structural rearrangement and suppresses the oxygen release at the end of the voltage plateau, in agreement with the better cyclability observed for Co00. The oxygen redox could, in fact, be affected by the amount of random stacking sequence of the layered structure, where low-defect samples are expected to convert faster to the spinel phase, while defective samples give access to higher capacities. Within this picture we hypothesize that Co00 is presenting a higher amount of random stacking sequences of the layered structure compared to Co08. Finally, the oxygen release and the concomitant local interlayer structural rearrangements occurring in Co08 at the end of the voltage plateau have been identified to occur close to the Mn sites.

ACKNOWLEGEMENTS

The authors acknowledge financial support from the Spanish State Research Agency (AEI), through the Severo Ochoa Programme for Centres of Excellence in R&D (CEX2023-001263-S), and the projects PID2021-124681OB-I00 and TED2021-132707B-I00.

REFERENCES

1. Haas J*, et al.* Challenges and trends of energy storage expansion planning for flexibility provision in low-carbon power systems – a review. *Renewable and Sustainable Energy Reviews* **80**, 603-619 (2017).

2. Ellabban O, Abu-Rub H, Blaabjerg F. Renewable energy resources: Current status, future prospects and their enabling technology. *Renewable and Sustainable Energy Reviews* **39**, 748-764 (2014).

3. Owusu PA, Asumadu-Sarkodie S. A review of renewable energy sources, sustainability issues and climate change mitigation. *Cogent Engineering* **3**, 1167990 (2016).

4. Panwar NL, Kaushik SC, Kothari S. Role of renewable energy sources in environmental protection: A review. *Renewable and Sustainable Energy Reviews* **15**, 1513-1524 (2011).

5. Camargos PH, dos Santos PHJ, dos Santos IR, Ribeiro GS, Caetano RE. Perspectives on Li-ion battery categories for electric vehicle applications: A review of state of the art. *International Journal of Energy Research* **46**, 19258-19268 (2022).

6. Mizushima K, Jones PC, Wiseman PJ, Goodenough JB. Li_xCoO_2 (0<x<-1): A new cathode material for batteries of high energy density. *Materials Research Bulletin* **15**, 783-789 (1980).

7. Olivetti EA, Ceder G, Gaustad GG, Fu X. Lithium-Ion Battery Supply Chain Considerations: Analysis of Potential Bottlenecks in Critical Metals. *Joule* **1**, 229-243 (2017).

8. Vaalma C, Buchholz D, Weil M, Passerini S. A cost and resource analysis of sodium-ion batteries. *Nature Reviews Materials* **3**, 18013 (2018).

9. Rozier P, Tarascon JM. Review — Li-Rich Layered Oxide Cathodes for Next-Generation Li-Ion Batteries: Chances and Challenges. *Journal of The Electrochemical Society* **162**, A2490 (2015).

10. Kim M-H, Shin H-S, Shin D, Sun Y-K. Synthesis and electrochemical properties of $Li[Ni_{0.8}Co_{0.1}Mn_{0.1}]O_2$ and $Li[Ni_{0.8}Co_{0.2}]O_2$ via co-precipitation. *Journal of Power Sources* **159**, 1328-1333 (2006).

11. Laszczynski N, von Zamory J, Kalhoff J, Loeffler N, Chakravadhanula VSK, Passerini S. Improved Performance of VO_x-Coated Li-Rich NMC Electrodes. *ChemElectroChem* **2**, 1768-1773 (2015).

12. Noh H-J, Youn S, Yoon CS, Sun Y-K. Comparison of the structural and electrochemical properties of layered $Li[Ni_xCo_yMn_z]O_2$ (x = 1/3, 0.5, 0.6, 0.7, 0.8 and 0.85) cathode material for lithium-ion batteries. *Journal of Power Sources* **233**, 121-130 (2013).

13. Buchholz D, Li J, Passerini S, Aquilanti G, Wang D, Giorgetti M. X-ray Absorption Spectroscopy Investigation of Lithium-Rich, Cobalt-Poor Layered-Oxide Cathode Material with High Capacity. *ChemElectroChem* **2**, 85-97 (2015).

14. Wang J, He X, Paillard E, Laszczynski N, Li J, Passerini S. Lithium- and Manganese-Rich Oxide Cathode Materials for High-Energy Lithium Ion Batteries. *Advanced Energy Materials* **6**, 1600906 (2016).

15. Liu Z, Yu A, Lee JY. Synthesis and characterization of $LiNi_{1-x-y}Co_xMn_yO_2$ as the cathode materials of secondary lithium batteries. *Journal of Power Sources* **81-82**, 416-419 (1999).

16. Ohzuku T, Makimura Y. Layered Lithium Insertion Material of $LiCo_{1/3}Ni_{1/3}Mn_{1/3}O_2$ for Lithium-Ion Batteries. *Chemistry Letters* **30**, 642-643 (2003).

17. Rosina KJ, Jiang M, Zeng D, Salager E, Best AS, Grey CP. Structure of aluminum fluoride coated Li $[Li_{1/9}Ni_{1/3}Mn_{5/9}]O_2$ cathodes for secondary lithium-ion batteries. *Journal of Materials Chemistry* **22**, 20602-20610 (2012).

18. Guan X, Ding B, Liu X, Zhu J, Mi C, Zhang X. Enhancing the electrochemical performance of $Li_{1.2}Ni_{0.2}Mn_{0.6}O_2$ by surface modification with nickel–manganese composite oxide. *Journal of Solid State Electrochemistry* **17**, 2087-2093 (2013).

19. Myung S-T*, et al.* Functionality of Oxide Coating for $Li[Li_{0.05}Ni_{0.4}Co_{0.15}Mn_{0.4}]O_2$ as Positive Electrode Materials for Lithium-Ion Secondary Batteries. *The Journal of Physical Chemistry C* **111**, 4061-4067 (2007).

20. Shi SJ*, et al.* Enhanced cycling stability of $Li[Li_{0.2}Mn_{0.54}Ni_{0.13}Co_{0.13}]O_2$ by surface modification of MgO with melting impregnation method. *Electrochimica Acta* **88**, 671-679 (2013).

21. Wu Y, Manthiram A. High Capacity, Surface-Modified Layered $Li[Li_{(1-x)/3}Mn_{(2-x)/3}Ni_{x/3}Co_{x/3}]O_2$ Cathodes with Low Irreversible Capacity Loss. *Electrochemical and Solid-State Letters* **9**, A221 (2006).

22. Zhao Y, Zhao C, Feng H, Sun Z, Xia D. Enhanced Electrochemical Performance of $Li[Li_{0.2}Ni_{0.2}Mn_{0.6}]O_2$ Modified by Manganese Oxide Coating for Lithium-Ion Batteries. *Electrochemical and Solid-State Letters* **14**, A1 (2011).

23. Zheng JM, Li J, Zhang ZR, Guo XJ, Yang Y. The effects of TiO_2 coating on the electrochemical performance of $Li[Li_{0.2}Mn_{0.54}Ni_{0.13}Co_{0.13}]O_2$ cathode material for lithium-ion battery. *Solid State Ionics* **179**, 1794-1799 (2008).

24. Ali SE*, et al.* Quantification of charge compensation in lithium- and manganese-rich Li-ion cathode materials by x-ray spectroscopies. *Materials Today Physics* **24**, 100687 (2022).

25. Luo K*, et al.* Charge-compensation in 3d-transition-metal-oxide intercalation cathodes through the generation of localized electron holes on oxygen. *Nature Chemistry* **8**, 684-691 (2016).

26. Seo D-H, Lee J, Urban A, Malik R, Kang S, Ceder G. The structural and chemical origin of the oxygen redox activity in layered and cation-disordered Li-excess cathode materials. *Nature Chemistry* **8**, 692-697 (2016).

27. Yu Y*, et al.* Towards controlling the reversibility of anionic redox in transition metal oxides for high-energy Li-ion positive electrodes. *Energy & Environmental Science* **14**, 2322-2334 (2021).

28. Ali SE*, et al.* Local Interactions Governing the Performances of Lithium- and Manganese-Rich Cathodes. *The Journal of Physical Chemistry Letters* **12**, 1195-1201 (2021).

29. Simonelli L*, et al.* Role of Manganese in Lithium- and Manganese-Rich Layered Oxides Cathodes. *The Journal of Physical Chemistry Letters* **10**, 3359-3368 (2019).

30. Black AP*, et al.* Synchrotron radiation based *operando* characterization of battery materials. *Chemical science* **14**, 1641-1665 (2023).

31. Fehse M, Iadecola A, Simonelli L, Longo A, Stievano L. The rise of X-ray spectroscopies for unveiling the functional mechanisms in batteries. *Physical Chemistry Chemical Physics* **23**, 23445-23465 (2021).

32. Li B*, et al.* Decoupling the roles of Ni and Co in anionic redox activity of Li-rich NMC cathodes. *Nature Materials* **22**, 1370-1379 (2023).

33. Li B*, et al.* Constructing “Li-rich Ni-rich” oxide cathodes for high-energy-density Li-ion batteries. *Energy & Environmental Science* **16**, 1210-1222 (2023).

34. Manthiram A, Knight JC, Myung S-T, Oh S-M, Sun Y-K. Nickel-Rich and Lithium-Rich Layered Oxide Cathodes: Progress and Perspectives. *Advanced Energy Materials* **6**, 1501010 (2016).

35. Wu F*, et al.* Elucidating the Effect of Iron Doping on the Electrochemical Performance of Cobalt-Free Lithium-Rich Layered Cathode Materials. *Advanced Energy Materials* **9**, 1902445 (2019).

36. Li J*, et al.* Synthesis and electrochemical performance of the high voltage cathode material $Li[Li_{0.2}Mn_{0.56}Ni_{0.16}Co_{0.08}]O_2$ with improved rate capability. *Journal of Power Sources* **196**, 4821-4825 (2011).

37. Kazzazi A, Bresser D, Birrozzi A, von Zamory J, Hekmatfar M, Passerini S. Comparative Analysis of Aqueous Binders for High-Energy Li-Rich NMC as a Lithium-Ion Cathode and the Impact of Adding Phosphoric Acid. *ACS Applied Materials & Interfaces* **10**, 17214-17222 (2018).

38. Simonelli L*, et al.* CLÆSS: The hard X-ray absorption beamline of the ALBA CELLS synchrotron. *Cogent Physics* **3**, 1231987 (2016).

39. Prins R, Koningsberger D. *X-ray absorption: principles, applications, techniques of EXAFS, SEXAFS, and XANES*. Wiley (1988).

40. Jaumot J, de Juan A, Tauler R. MCR-ALS GUI 2.0: New features and applications. *Chemometrics and Intelligent Laboratory Systems* **140**, 1-12 (2015).

41. de Juan A, Tauler R. Chapter 2 - Multivariate Curve Resolution-Alternating Least Squares for Spectroscopic Data. In: *Data Handling in Science and Technology* (ed Ruckebusch C). Elsevier (2016).

42. Newville M. Larch: An Analysis Package for XAFS and Related Spectroscopies. *Journal of Physics: Conference Series* **430**, (2013).

43. Sorrentino A*, et al.* MISTRAL: a transmission soft X-ray microscopy beamline for cryo nano-tomography of biological samples and magnetic domains imaging. *Journal of Synchrotron Radiation* **22**, 1112-1117 (2015).

44. Otón J, Sorzano COS, Marabini R, Pereiro E, Carazo JM. Measurement of the modulation transfer function of an X-ray microscope based on multiple Fourier orders analysis of a Siemens star. *Opt Express* **23**, 9567-9572 (2015).

45. Koyama Y, Arai H, Ogumi Z, Tanaka I, Uchimoto Y. Co *K*-edge XANES of $LiCoO_2$ and CoO_2 with a variety of structures by supercell density functional calculations with a core hole. *Physical Review B* **85**, 075129 (2012).

46. Serrano-Sevillano J*, et al.* Enhanced electrochemical performance of Li-rich cathode materials through microstructural control. *Physical Chemistry Chemical Physics* **20**, 23112-23122 (2018).

47. Li X*, et al.* Rational design of thermally stable polymorphic layered cathode materials for next generation lithium rechargeable batteries. *Materials Today* **61**, 91-103 (2022).

48. Hu E*, et al.* Evolution of redox couples in Li- and Mn-rich cathode materials and mitigation of voltage fade by reducing oxygen release. *Nature Energy* **3**, 690-698 (2018).